Physica Medica 68 (2019) 17–34

Contents lists available at ScienceDirect

Physica Medica

journal homepage: www.elsevier.com/locate/ejmp

Original paper

Geant4 Monte Carlo investigation of the magnetic field effect on dose distributions in low-density regions in magnetic resonance image-guided radiation therapy

Masayuki Yano[a], Fujio Araki[b,*], Takeshi Ohno[b]

[a] Graduate School of Health Sciences, Kumamoto University, 4-24-1 Kuhonji, Chuo-ku, Kumamoto 862-0976, Japan
[b] Department of Health Sciences, Faculty of Life Sciences, Kumamoto University, 4-24-1 Kuhonji, Chuo-ku, Kumamoto 862-0976, Japan

ARTICLE INFO

Keywords:
Transverse and longitudinal magnetic field
Low density
Dose distributions
Electron return effect
Monte Carlo method

ABSTRACT

It is necessary to evaluate the effect of the presence of a magnetic field when treating lung tumors with MRIgRT. In this study, the effect of transverse and longitudinal magnetic fields on dose distributions in low-density regions was quantitatively investigated. The dose distributions in a virtual lung phantom under the influence of magnetic fields were calculated using the Geant4 Monte Carlo code. The phantom size was 30 × 20 × 30 cm^3, and it was composed of three layers: water (3 cm thickness), lung (12 cm thickness), and water (5 cm thickness). The density of the lung layer was set to 0.1, 0.3 and 0.6 g/cm^3. The uniform magnetic flux densities of 0.35 T and 1.5 T were used for 2 × 2, 5 × 5, and 10 × 10 cm^2 fields at a source-to-surface distance of 100 cm, using a 6 MV photon spectrum. The dose at the water–lung interface in a lung phantom increased by 58%, 51%, and 22% for the lung densities of 0.1, 0.3, and 0.6 g/cm^3, respectively. In the 1.5 T longitudinal magnetic field, the penumbra at the lung center (at the depth of 9 cm) decreased by 5.14, 1.50 and 0.35 mm for a 5 × 5 cm^2 field, respectively. The dose distributions in lowdensity regions are more affected by the magnetic field. In conclusion, the doses at the water–lung interface increased in the transverse magnetic field. The depth dose increased, and the penumbra decreased in the longitudinal magnetic field.

1. Introduction

In recent years, magnetic resonance image-guided radiation therapy (MRIgRT) systems that combine a linear accelerator (linac) and a magnetic resonance (MR) scanner have been developed in Europe and the United States. The MRIgRT systems provide excellent contrast images between a tumor and the surrounding soft tissues. Further, it is possible to observe the tumor movement with respiratory motion in real time. This makes it possible to reduce the tumor margins defined in the treatment planning, effectively irradiating the tumor while suppressing the dose to normal tissues. Thus, the local control rate of the tumor is expected to improve with higher precision positioning.

The MRIgRT systems currently being studied and developed, are classified in two types. One system has the transverse magnetic field to the beam axis; ViewRay has developed radiotherapy units combining three ^{60}Co sources or 6 MV linac and 0.35 T MRI [1], and Elekta has developed the unit combining 7 MV linac and 1.5 T MRI [2]. In the transverse magnetic field, charged particles are deflected by the Lorentz force. It has been reported that the dose increases on the exit surface owing to the "electron return effect (ERE)" [3–5]. In addition, the presence of a magnetic field has the effect of shifting the dose distributions along the direction of the Lorentz force [6–9]. The other system is the longitudinal magnetic field to the beam axis; MagnetTx has combined a 6 MV linac and 0.5 T MRI [10], and Australian MRI-Linac has combined 4 MV or 6 MV linac and 1.0 T MRI [11]. Effects such as the ERE do not appear in this case. However, it has been demonstrated that incident electrons from the upper side of the multileaf collimator (MLC) travel along the beam axis, thereby increasing the skin dose in the patient [12–17].

In the patient's body, in lowdensity tissues, such as the lung, the electron ranges are longer; hence the influence of the magnetic field strength is greater than in other tissues (e.g. soft tissue). It has been reported that the lung density changes with the patient's age, health condition, and respiratory phase [18,19]. In this study, the influence of the transverse and longitudinal magnetic field strength on dose distributions for various lung densities was quantitatively investigated by comparing the percentage depth doses (PDDs) and lateral dose profiles, using the Geant4 Monte Carlo (MC) code. The effect of both magnetic

* Corresponding author.
E-mail address: f_araki@kumamoto-u.ac.jp (F. Araki).

https://doi.org/10.1016/j.ejmp.2019.11.005
Received 12 March 2019; Received in revised form 15 October 2019; Accepted 2 November 2019
Available online 12 November 2019

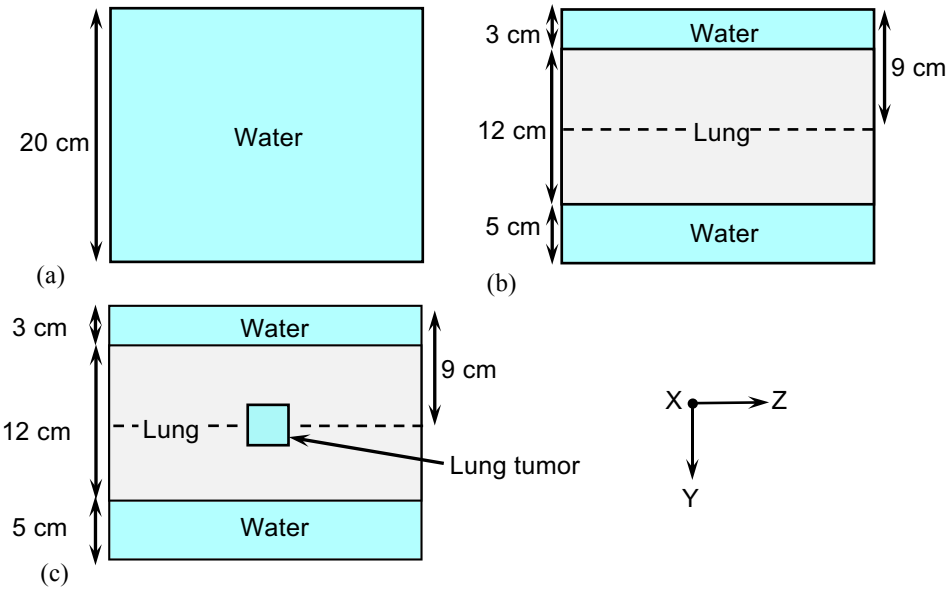

Fig. 1. Schematic geometry of virtual phantoms: (a) water, (b) lung, and (c) lung tumor.

Table 1
Fraction by weight for the elemental composition of water and lung tissue modelled in the Geant4 simulation.

Phantom	Composition (%)								
	H	C	N	O	Na	P	S	Cl	Ka
Water	11.2	–	–	88.8	–	–	–	–	–
Lung	10.3	10.5	3.1	74.9	0.2	0.2	0.3	0.3	0.2

Table 2
Cut-off ranges equivalent to cut-off energies of 10 keV for photons and 521 keV for electrons in water and lung phantoms.

Phantom	Density (g/cm^3)	Cutoff range (mm)	
		Photon	Electron
Water	1.0	18.1	0.38
Lung	0.1	188	3.90
	0.3	62.5	1.30
	0.6	31.2	0.65

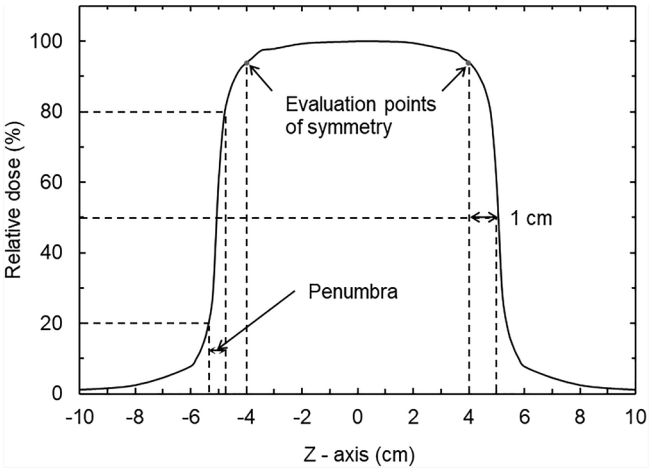

Fig. 2. Symmetry and penumbra in lateral dose profile at Z-axis shown in Fig. 1.

field strengths on dose distributions at the water (or tumor)–lung or lung–water (or tumor) interface was also analyzed.

2. Materials and methods

2.1. Monte Carlo simulations

Geant4 (GEometry ANd Tracking) version 10.2 was used as Monte Carlo code [20–22]. FTFP_BERT was adopted as physics list; we based our decision on its computational efficiency and the fact that it provided enough accuracy for the purpose of this study. The dose was scored by using the command-based scoring. The command-based scoring is a technique of dividing and scoring a parallel world that can be defined independently from mass geometry defined by the Geant4 structure geometry [22]. Three virtual phantoms were modelled in the Geant4 simulation: water, lung, and lung tumor phantom (Fig. 1). The water phantom sizes were $30 \times 20 \times 30\,cm^3$ and the lung phantom was composed of three layers: water (3 cm thickness), lung (12 cm thickness), and water (5 cm thickness). The thickness is in the direction of the photon beam. The density of the lung layer was set to 0.1, 0.3,

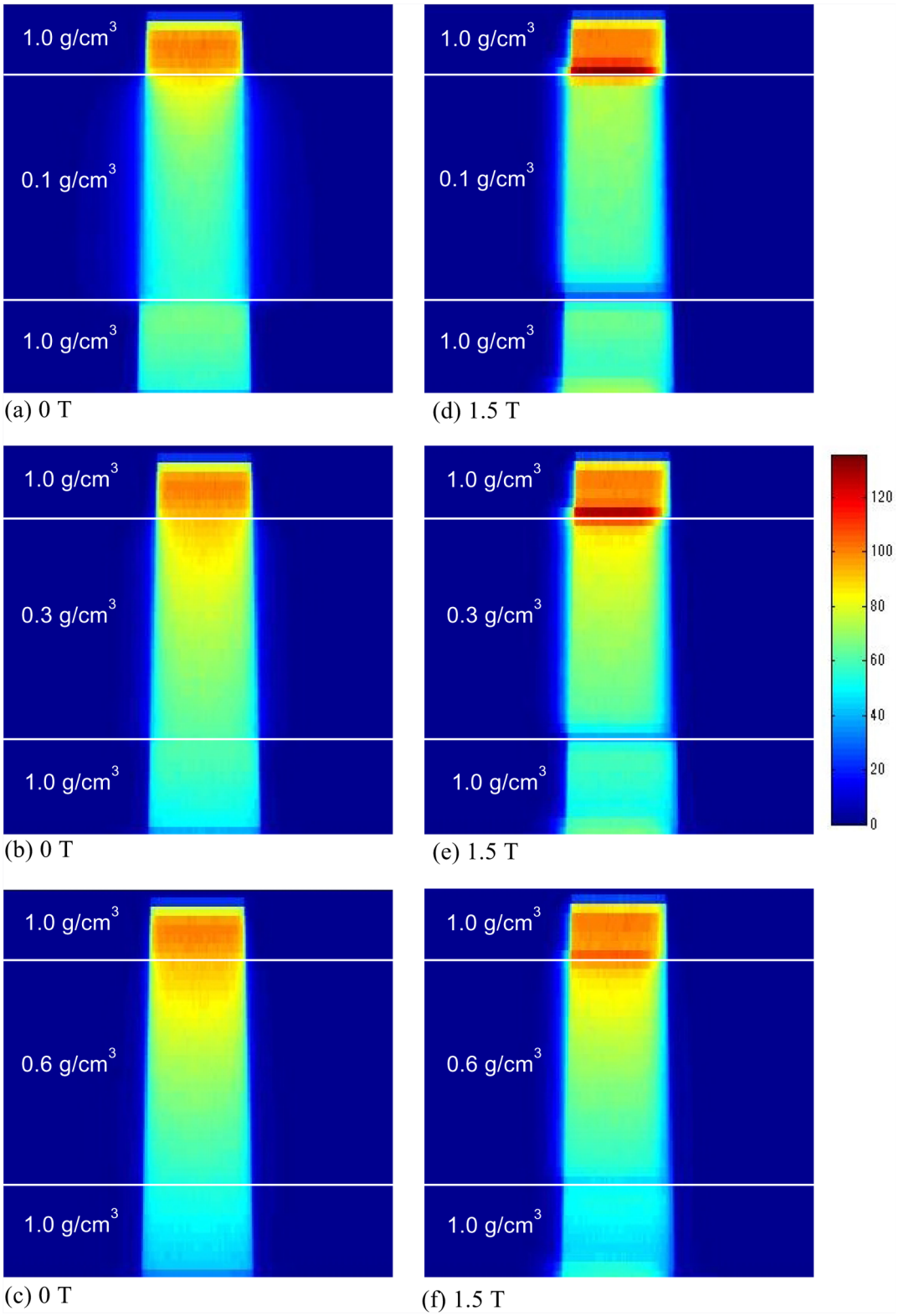

Fig. 3. Comparison of dose distributions in the transverse magnetic field of 0 T and 1.5 T for a 5 × 5 cm^2 field in lung densities of 0.1, 0.3, and 0.6 g/cm^3 at SSD of 100 cm.

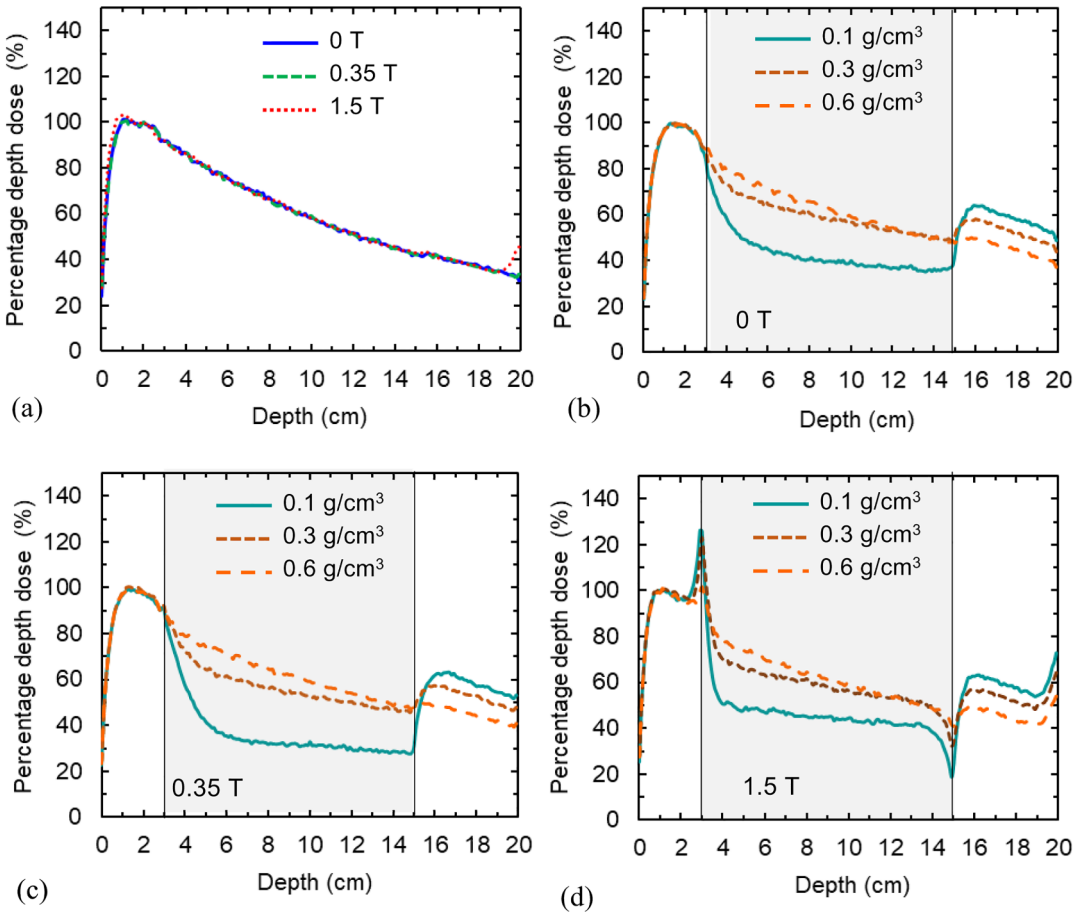

Fig. 4. Comparison of PDDs in transverse magnetic flux density: (a) 0, 0.35, and 1.5 T for a 2 × 2 cm^2 field in a water phantom at SSD of 100 cm, (b) 0 T, (c) 0.35 T, and (d) 1.5 T in lung phantoms with densities of 0.1, 0.3, and 0.6 g/cm^3.

and 0.6 g/cm^3. In addition, the lung tumor size was set to 3 × 3 × 3 cm^3 and placed at a depth of 9 cm inside the lung phantom. Table 1 shows the composition of the water and lung phantoms modelled by the Geant4 simulation. The lung tumor was modelled with water [8]. Table 2 shows cutoff ranges of photons and electrons for water and lung phantoms. The cut-off ranges are equivalent to cut-off energies of 10 keV for photons and 521 keV (includes the rest energy) for electrons.

2.2. Dose distribution calculations

The 6 MV photon spectrum from a Varian iX linac (Varian Medical Systems) was irradiated with 2 × 2, 5 × 5, and 10 × 10 cm^2 fields at a source-to-surface distance (SSD) of 100 cm. The photon spectrum was obtained from phase space file scored for a 10 × 10 cm^2 field at SSD of 100 cm using the EGSnrc Monte Carlo code [23]. The phase space file has been calculated in the previous studies [24,25]. The mean photon energy was 1.99 MeV for 2 × 2 cm^2 and 1.87 MeV for 10 × 10 cm^2 and it was little difference. Thus, the spectrum for 10 × 10 cm^2 field was used for all calculations. The uniform transverse or longitudinal magnetic field was applied in the irradiation direction (beam axis). The dose distributions in the phantoms presented in Fig. 1 were calculated for the magnetic flux densities of 0, 0.35, and 1.5 T. The number of incident particles for all cases was set to 4.0 × 10^8, and the statistical uncertainty in the calculated doses was less than 1%.

The influence of the magnetic field strength for dose distributions in various lung densities was compared in terms of PDDs and lateral dose profiles at a depth of 9 cm. The dose was obtained by using command-based scoring with a voxel size of 5 × 1 × 5 mm^3 for PDDs and 5 × 5 × 1 mm^3 for dose lateral profiles. In addition, PDDs and lateral dose profiles were normalized to the absorbed dose at a depth of 1.5 cm in the case of an irradiation without the magnetic field. Further, the symmetry of lateral dose profiles with and without magnetic fields was evaluated for different lung densities for 5 × 5 and 10 × 10 cm^2 fields. The symmetry was evaluated by calculating the ratio of doses in two points that were set to 1 cm inside the field edges (50% dose) on

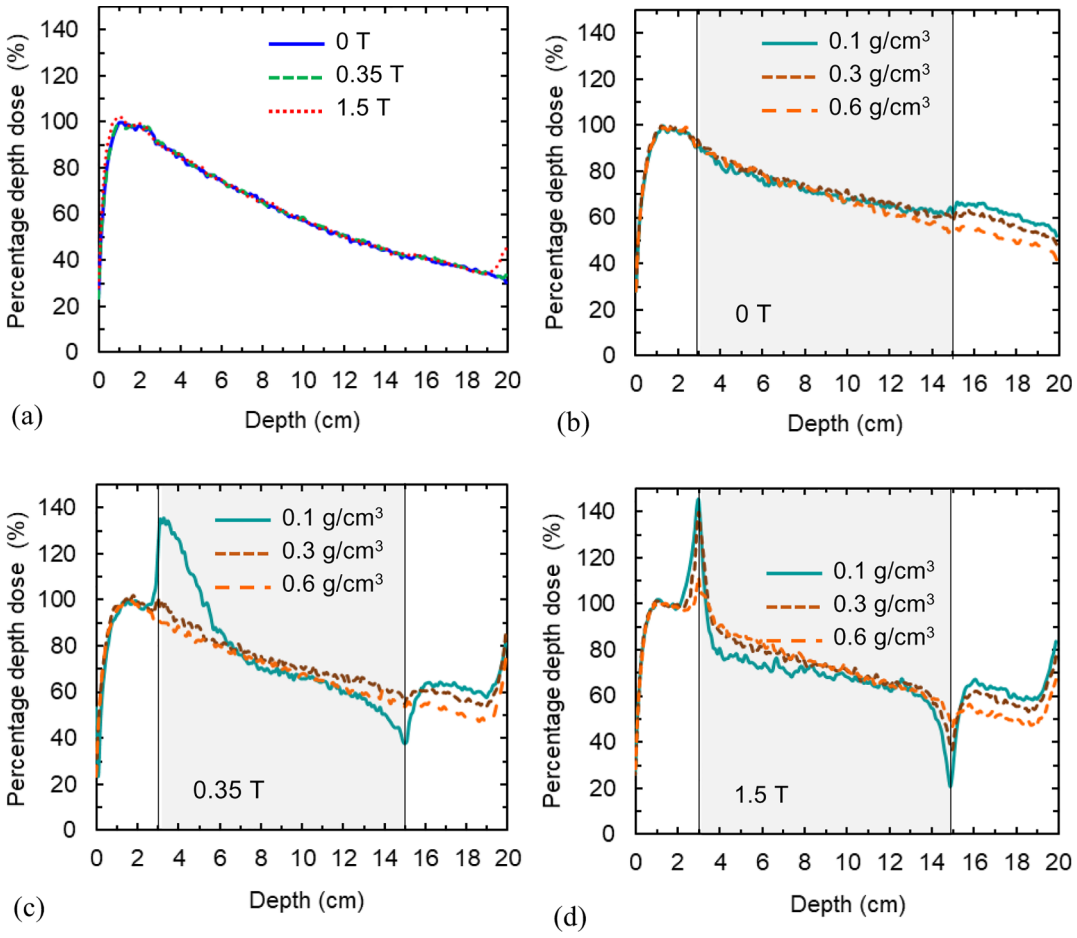

Fig. 5. Comparison of PDDs in transverse magnetic flux density: (a) 0, 0.35, and 1.5 T for a 10 × 10 cm^2 field in a water phantom at SSD of 100 cm, (b) 0 T, (c) 0.35 T, and (d) 1.5 T in lung phantoms with densities of 0.1, 0.3, and 0.6 g/cm^3.

opposite side of the central beam axis as shown in Fig. 2. Finally, in order to investigate the impact of dose profiles owing to the longitudinal magnetic field, the penumbra was obtained from the following equation.

$$X = |X_{80} - X_{20}| \quad (1)$$

where X is the penumbra width (mm), X_{80} and X_{20} are the position (mm) at the dose of 80% and 20% at Z-axis, respectively (Fig. 2).

3. Results

3.1. Dose distributions with transverse magnetic field

Fig. 3(a)–(c) and (d)–(f) show dose distributions for the transverse magnetic field conditions of 0 T and 1.5 T in a 5 × 5 cm^2 field, respectively, for lung densities of 0.1, 0.3, and 0.6 g/cm^3 at SSD of 100 cm. It can be observed that the dose profiles in a 1.5 T magnetic field were more deflected toward the lateral direction for lower densities and higher magnetic fields owing to the Lorentz force.

Fig. 4(a)–(d) show a comparison of PDDs for the transverse magnetic flux densities of 0, 0.35, and 1.5 T in a 2 × 2 cm^2 field in virtual phantoms at SSD of 100 cm. In the water phantom, the exit surface dose increased by 47% for the 1.5 T condition, compared to the condition without magnetic field (Fig. 4(a)). The dose at the water–lung interface for the 1.5 T condition increased by 51%, 41%, and 15% in lung phantoms with densities of 0.1, 0.3, and 0.6 g/cm^3, respectively, compared to the condition without magnetic field (Fig. 4(d)). In contrast, the dose at the lung–water interface in 1.5 T decreased by 44%, 33%, and 14%, and the exit surface dose increased by 50%, 46%, and 46%, respectively. However, the dose distributions in the lung center were more distorted for 0.35 T than for 1.5 T, and the dose in 0.35 T decreased by 21%, 3.4% and 0.4%, with densities of 0.1, 0.3, and 0.6 g/cm^3, respectively.

Similarly, Fig. 5(a)–(d) present a comparison of PDDs for the 10 × 10 cm^2 field. The lateral electron equilibrium in this case is established even in the low-density region as shown in Fig. 5(a). In Fig. 5(c) and (d), the dose at the water–lung interface and the exit dose rapidly increased for lower densities and higher magnetic field

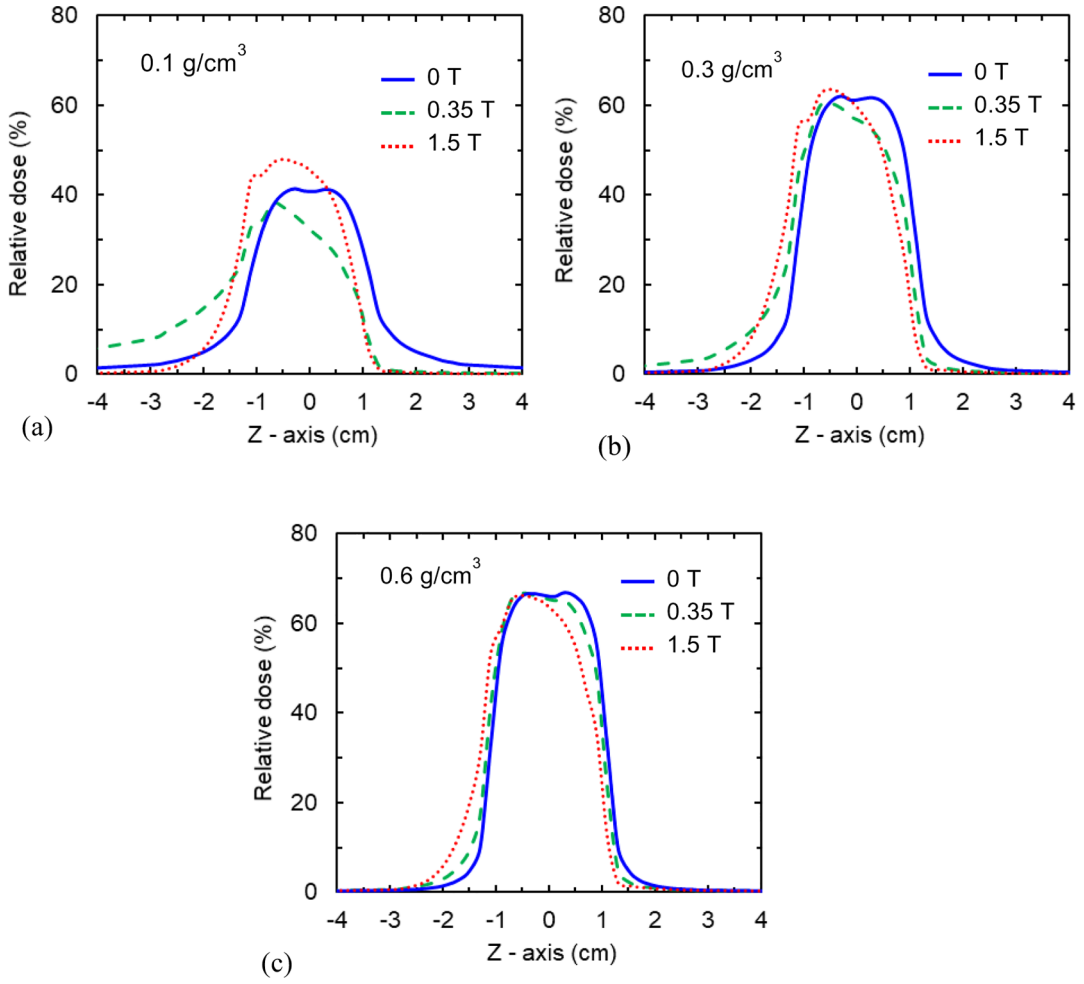

Fig. 6. Comparison of dose profiles by transverse magnetic fields for a 2 × 2 cm^2 field at SSD of 100 cm: densities of (a) 0.1 g/cm^3, (b) 0.3 g/cm^3, and (c) 0.6 g/cm^3 at a depth of 9 cm in a lung phantom. (Z-axis is defined in Fig. 1.)

magnitudes, unlike those of a 2 × 2 cm^2 field. Inversely, the dose at the lung–water interface rapidly decreased for lower densities and higher magnetic field magnitudes. The dose in the lung center was approximately the same for the 0 T, 0.35 T, and 1.5 T field conditions.

Fig. 6(a)–(c) show a comparison of the dose profiles at the lung center (depth of 9 cm) for the transverse magnetic flux densities of 0, 0.35, and 1.5 T in a 2 × 2 cm^2 field. The lower the magnetic flux density and the lung density, the worse was the symmetry of the dose profiles. The distortions in the dose profiles were caused by the Lorentz force. Similarly, Fig. 7(a)–(c) present a comparison of the dose profiles at the lung center in a 10 × 10 cm^2 field. The tendency of the dose profile distortion was similar to those for a 2 × 2 cm^2 field; however, the dose at the lung center was approximately the same for 0 T, 0.35 T, and 1.5 T field conditions. Table 3 presents a comparison of the symmetry of dose profiles for lung densities in transverse magnetic flux densities of 0 T, 0.35 T, and 1.5 T. The greatest influence was observed in densities of 0.1 g/cm^3 at 0.35 T for 5 × 5 and 10 × 10 cm^2 fields.

Figs. 8(a)–(d) and 9(a)–(d) present a comparison of dose profiles at water–lung and lung–water interfaces in transverse magnetic flux densities of 0.35 T and 1.5 T for 2 × 2 and 10 × 10 cm^2 fields. For densities of 0.1 and 0.3 g/cm^3, the dose profiles at the water–lung interface were remarkably deflected by ERE at 1.5 T compared to 0.35 T and produced the dose enhancement. In contrast, the dose profiles at the water–lung interface more decreased by ERE at 1.5 T than at 0.35 T.

Table 4 summarizes the dose increase/decrease at the water–lung interface (W-L), lung center (LC), and lung–water (L-W) interface in the transverse magnetic flux density for field sizes compared to 0 T.

3.2. Dose distributions with longitudinal magnetic field

Fig. 10(a)–(c) and (d)–(f) present the dose distributions for the longitudinal magnetic fields of 0 T and 1.5 T, respectively, a 5 × 5 cm^2 field, and lung densities of 0.1, 0.3, and 0.6 g/cm^3 at SSD of 100 cm. The penumbra of the dose distributions for the 1.5 T magnetic field

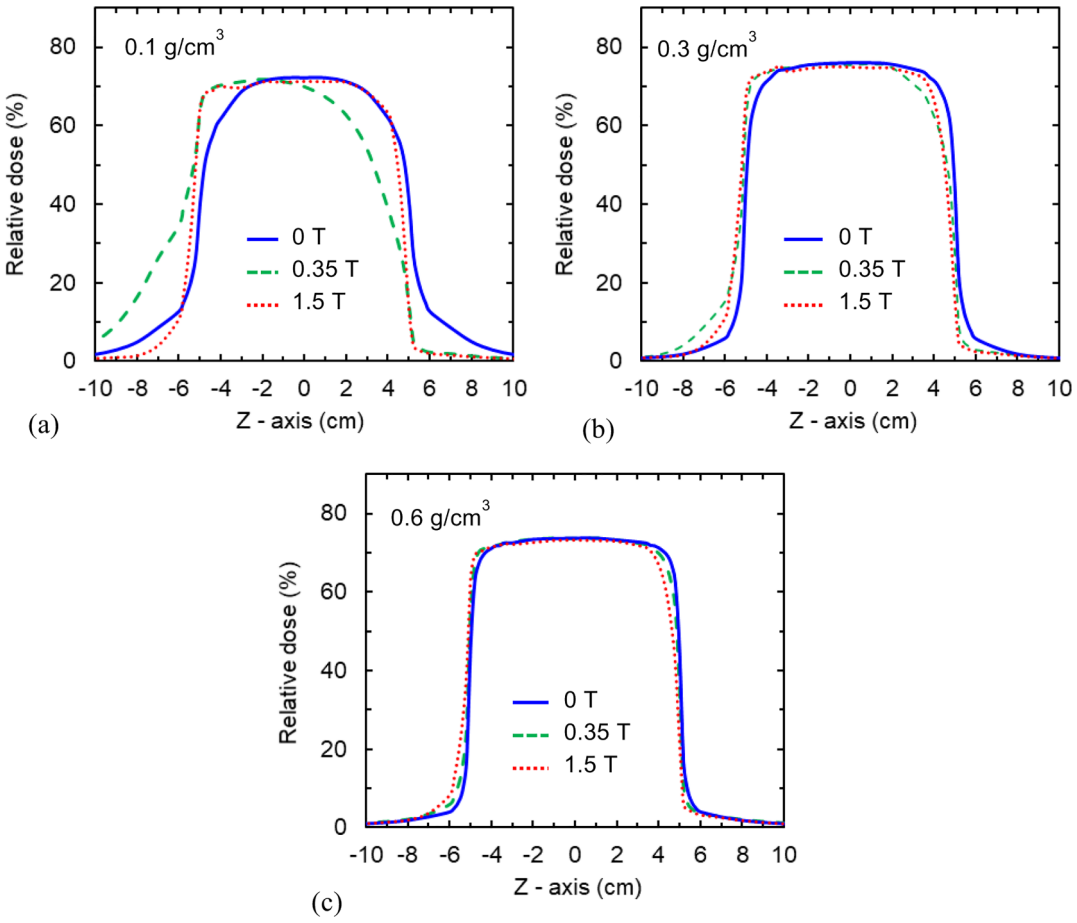

Fig. 7. Comparison of dose profiles by transverse magnetic fields for a 10 × 10 cm^2 field at SSD of 100 cm: densities of (a) 0.1 g/cm^3, (b) 0.3 g/cm^3, and (c) 0.6 g/cm^3 at a depth of 9 cm in a lung phantom. (Z-axis is defined in Fig. 1.)

Table 3
Comparison of the symmetry of dose profiles for lung densities in transverse magnetic flux densities of 0 T, 0.35 T, and 1.5 T at 5 × 5 and 10 × 10 cm^2 fields.

	5 × 5 cm^2			10 × 10 cm^2		
	0.1 g/cm^3	0.3 g/cm^3	0.6 g/cm^3	0.1 g/cm^3	0.3 g/cm^3	0.6 g/cm^3
0 T	1.00	1.00	1.00	1.00	1.00	1.00
0.35 T	1.94	1.26	1.04	1.81	1.17	1.02
1.5 T	1.27	1.26	1.15	1.11	1.11	1.06

decreased, and the depth dose increased for lower lung densities and higher magnetic field strengths owing to the Lorentz force. Here it should note that the dose in the buildup region dose not increase by the magnetic field because the photon fluence spectrum does not include the electron contamination from the linac head.

Fig. 11(a)–(c) show a comparison of PDDs for the longitudinal magnetic flux density of 0, 0.35, and 1.5 T in a 2 × 2 cm^2 field. In the water phantom, the variation of PDDs for the longitudinal magnetic field was quite small. The dose changes observed at the water–lung and lung–water interfaces and the exit surface for the transverse magnetic field were not seen for the longitudinal magnetic field condition. The dose at the lung center (depth of 9 cm) for the 1.5 T field condition

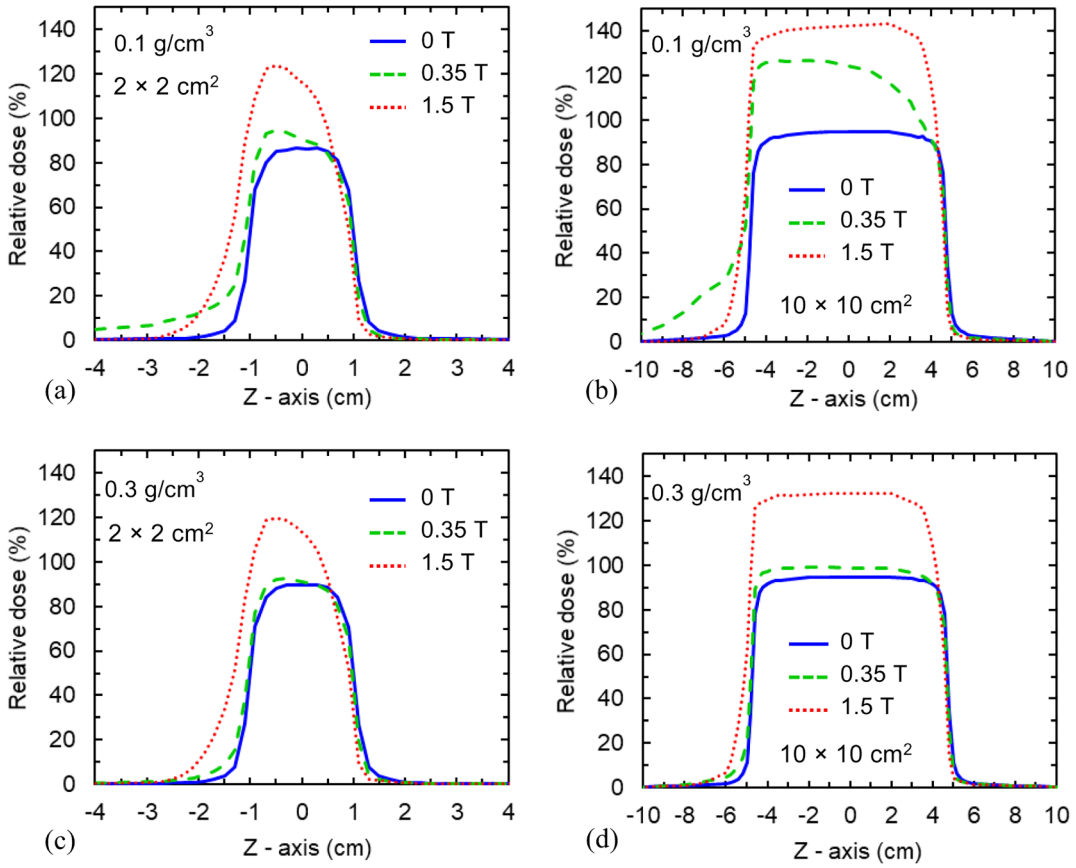

Fig. 8. Comparison of dose profiles at a water–lung interface (at depth of 3 cm) in transverse magnetic fields at SSD of 100 cm. (a) 2 × 2 cm^2 field in density of 0.1 g/cm^3, (b) 10 × 10 cm^2 and 0.1 g/cm^3, (c) 2 × 2 cm^2 and 0.3 g/cm^3, (d) 10 × 10 cm^2 and 0.3 g/cm^3. (Z-axis is defined in Fig. 1.)

increased by 97%, 21%, and 4% for lung densities of 0.1, 0.3, and 0.6 g/cm^3, respectively, compared to the condition without the magnetic field [Fig. 11(c)]. Fig. 12(a)–(d) present a comparison of PDDs for a 10 × 10 cm^2 field. Because the lateral electron equilibrium is established in low-density regions, the lung dose increased for lower densities and higher magnetic field strengths [Fig. 12(b) and (c)]. The lung dose for a 10 × 10 cm^2 field was enhanced more at 1.5 T than at 0.35 T. The dose at the lung center for 1.5 T increased by 18%, 3%, and 0.8% for lung densities of 0.1, 0.3, and 0.6 g/cm^3, respectively, compared to 0 T. The lung dose enhancement was effective in a small field of 2 × 2 cm^2 for 1.5 T.

Figs. 13(a)–(c) and 14(a)–(c) show the dose profiles for the 2 × 2 cm^2 and 10 × 10 cm^2 fields, respectively, at the lung center (depth of 9 cm), for the magnetic flux densities of 0, 0.35, and 1.5 T. The penumbra obtained from Eq. (1) for the 1.5 T longitudinal magnetic fields for a 5 × 5 cm^2 field decreased by 5.14 mm, 1.50 mm, and 0.35 mm for lung densities of 0.1, 0.3, and 0.6 g/cm^3, respectively, compared to the condition without the magnetic field, as shown in Table 5. Similarly, the penumbra for a 10 × 10 cm^2 field decreased by 8.03, 1.75, and 0.43 mm and remarkably decreased than the values for a 5 × 5 cm^2 field.

Table 6 summarizes the dose increase/decrease at the water–lung interface (W-L), lung center (LC), and lung–water (L-W) interface in the longitudinal magnetic flux density for field sizes compared to 0 T.

3.3. Dose distributions in lung tumor phantom

Fig. 15 shows a comparison of PDDs and dose profiles in a lung tumor phantom with the lung density of 0.3 g/cm^3, for 0 T and 1.5 T transverse and longitudinal magnetic fields, respectively, for a 5 × 5 cm^2 field at SSD of 100 cm. The PDDs and dose profiles greatly varied by ERE at each interface in the transverse magnetic field. It is difficult to deliver effective dose in the tumor anymore. The dose distributions were deflected to the left direction by the Lorentz force. In contrast, the dose distributions in the longitudinal magnetic field were slightly enhanced at the lung–tumor interface. The penumbra for the 1.5 T longitudinal magnetic field reduced by 1.5 mm compared to the condition without the magnetic field.

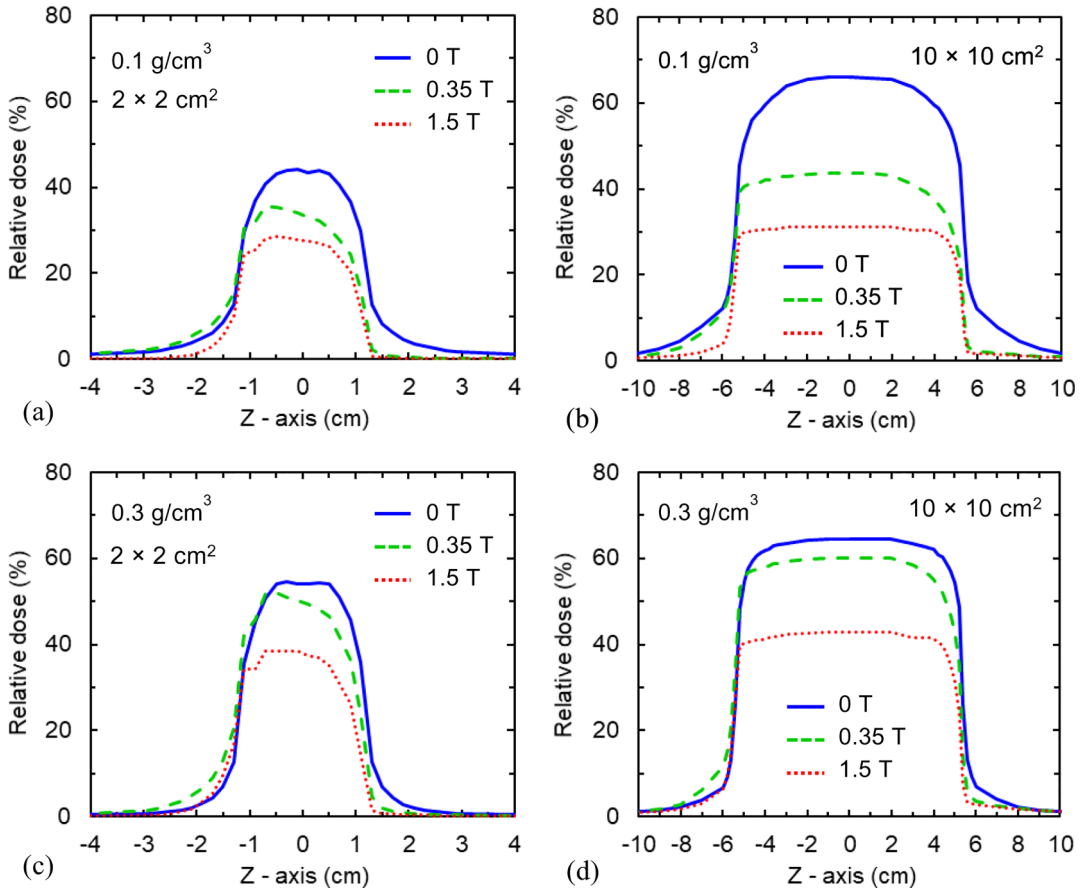

Fig. 9. Comparison of dose profiles at a lung–water interface (at depth of 15 cm) in transverse magnetic fields at SSD of 100 cm. (a) 2 × 2 cm^2 field in density of 0.1 g/cm^3, (b) 10 × 10 cm^2 and 0.1 g/cm^3, (c) 2 × 2 cm^2 and 0.3 g/cm^3, (d) 10 × 10 cm^2 and 0.3 g/cm^3. (Z-axis is defined in Fig. 1.)

Table 4
Dose increase/decrease at the water–lung interface (W-L), lung center (LC), and lung–water (L-W) interface in the transverse magnetic flux density for field sizes compared to 0 T.

Field (cm^2)	Magnetic flux density (T)	Density (g/cm^3)	Dose increase/decrease for 0 T		
			W-L	LC	L-W
2 × 2	0.35	0.1	8.4	−20.8	−25.5
		0.3	4.9	−3.4	−7.8
		0.6	0.8	−0.4	−0.9
	1.5	0.1	50.9	12.7	−44.3
		0.3	40.5	1.2	−33.4
		0.6	14.8	−2.2	−14.2
5 × 5	0.35	0.1	27.5	−13.8	−32.1
		0.3	6.4	−2.4	−8.7
		0.6	2.3	0.6	−2.3
	1.5	0.1	62.6	13.6	−54.2
		0.3	50.6	1.0	−36.7
		0.6	20.0	−0.3	−14.3
10 × 10	0.35	0.1	31.4	−0.8	−39.0
		0.3	8.5	4.4	−6.0
		0.6	2.2	−0.9	−1.3
	1.5	0.1	57.9	−2.5	−57.8
		0.3	50.5	3.3	−36.9
		0.6	22.1	4.3	−14.1

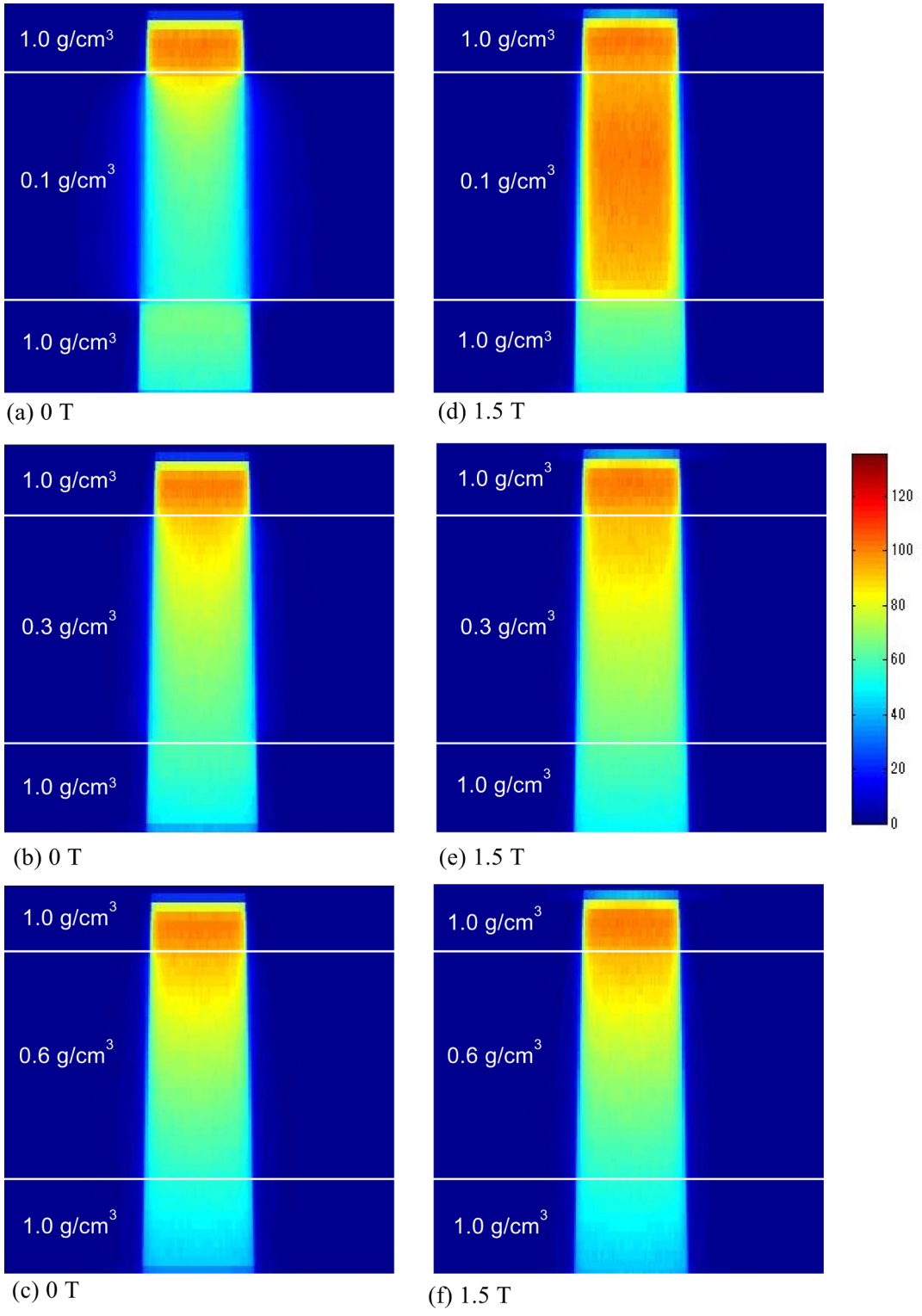

Fig. 10. Comparison of dose distributions in the longitudinal magnetic field of 0 T and 1.5 T for a 5 × 5 cm^2 field in lung densities of 0.1, 0.3, and 0.6 g/cm^3 at SSD of 100 cm.

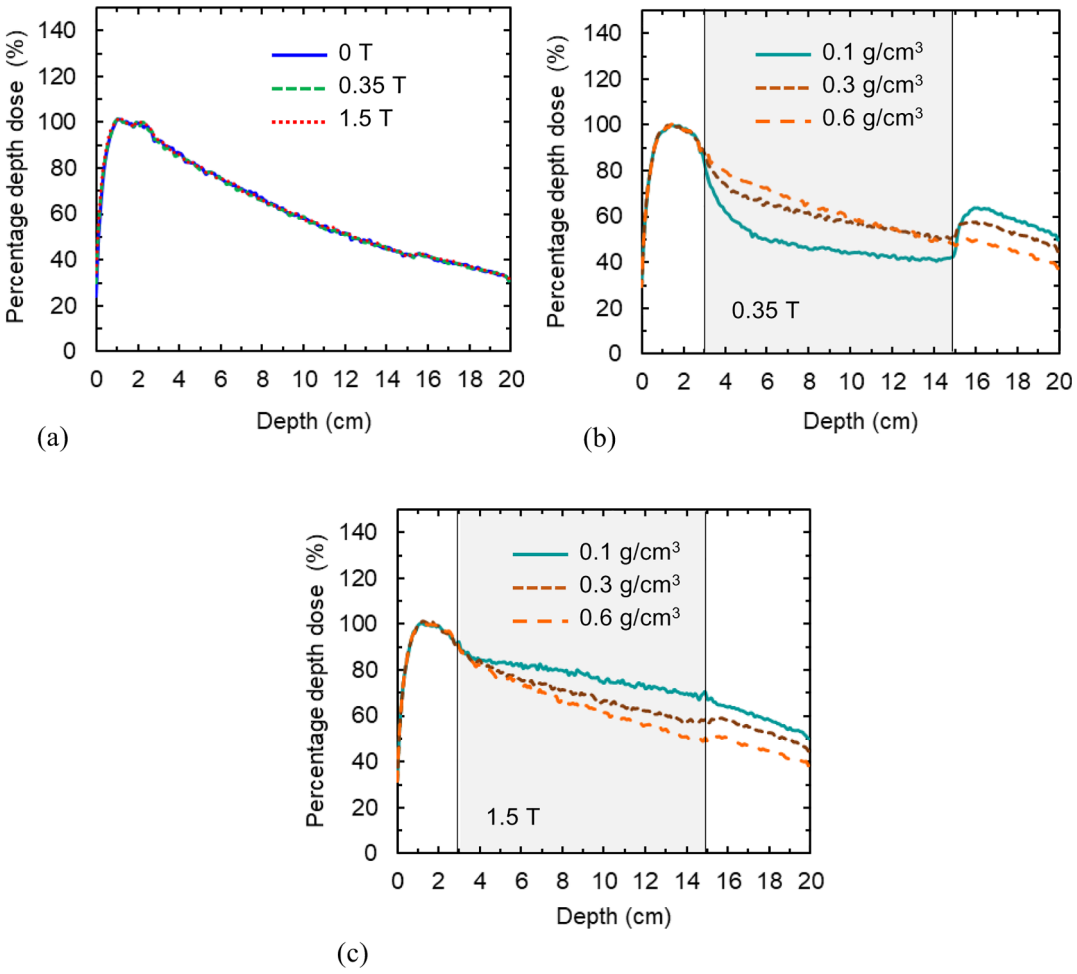

Fig. 11. Comparison of PDDs by longitudinal magnetic flux density for a 2 × 2 cm^2 field at SSD of 100 cm: (a) 0, 0.35, and 1.5 T in a water phantom, (b) 0.35 T and (c) 1.5 T in lung phantoms with densities of 0.1, 0.3, and 0.6 g/cm^3.

4. Discussion

4.1. Dose distributions with transverse magnetic field

Fig. 16(a)–(d) present the trajectory of secondary electrons generated by the photon interactions in a lung phantom for transverse magnetic flux density of 0.35 T. The gyro radius of secondary electrons is obtained from the following equation:

$$r = \frac{m\nu}{eB}, \tag{2}$$

where r is the gyro radius of secondary electrons (m), m is electron mass (kg), ν is electron velocity (m/s), e is the electric charge of the electron, and B is the magnetic flux density (T). In the transverse magnetic field scenario, secondary electrons entering water from lung and air, return to water by the ERE [3–5]. The gyro radius for an electron with the mean energy of 1.34 MeV is 1.70 cm for a 0.35 T field and 0.40 cm for a 1.5 T field, according to Eq. (2). The mean electron energy of 1.34 MeV was obtained from the electron fluence spectrum of a 5 × 5 cm^2 field using the EGSnrc/flurznrc code [23]. In this case, the 6 MV photon spectrum at a 10 × 10 cm^2 field was used as an incident photon beam. The electron range is 5.93, 1.98, and 0.99 cm in lung densities of 0.1, 0.3, and 0.6 g/cm^3, respectively, and 0.59 cm in water of 1.0 g/cm^3. That is, trajectories of secondary electrons in the lung are determined by the gyro radius and the electron range.

Secondary electrons incident on lung from water and on air from water, suffer the action of the Lorentz force, and the smaller is the gyro radius, the more secondary electrons return to the interface. Therefore, the doses at the water–lung interface and exit surface remarkably

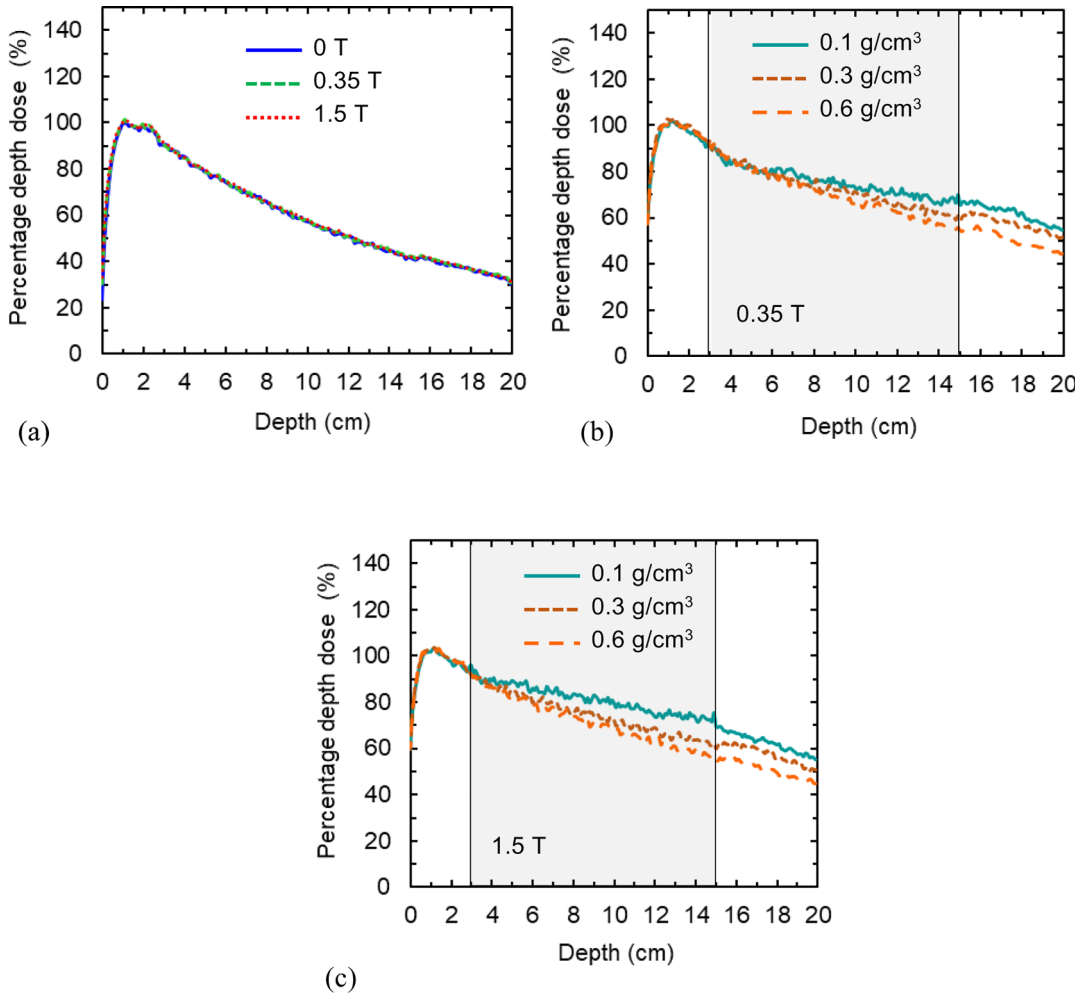

Fig. 12. Comparison of PDDs by longitudinal magnetic flux density for a 10 × 10 cm^2 field at SSD of 100 cm: (a) 0, 0.35, and 1.5 T in a water phantom, (b) 0.35 T and (c) 1.5 T in lung phantoms with densities of 0.1, 0.3, and 0.6 g/cm^3.

increases by ERE for the magnetic flux density of 1.5 T, as observed in Fig. 3(d)–(f). The ERE peak in lung was observed at a position distant from the central axis of approximately 0.5 cm for 2 × 2 cm^2 field in 1.5 T (Fig. 6). This almost corresponds to the gyro radius of secondary electrons for 1.5 T. The dose profiles with ERE in lung are deflected depending on the gyro radius and the range of secondary electrons. Especially, the dose profiles for 0.35 T are remarkably deflected for smaller fields in lower density region and consequently the secondary electrons get out of field shape [Table 4, Figs. 6(a) and 16(b)].

In contrast, the dose at the lung–water interface rapidly decreases because the secondary electrons cannot reach the boundary surface because of the Lorentz force action, unlike the trajectory of secondary electrons for 0 T. In addition, the ERE from water is very small owing to the short electron range in water. The smaller the lung density, the longer the electron range. Consequently, the influence of the magnetic field is remarkably more evident at lower densities.

4.2. Dose distributions with longitudinal magnetic field

Fig. 17(a)–(d) show the trajectory of secondary electrons enhanced by the photon interactions in a lung phantom for a longitudinal magnetic flux density of 1.5 T. In the longitudinal magnetic field scenario,

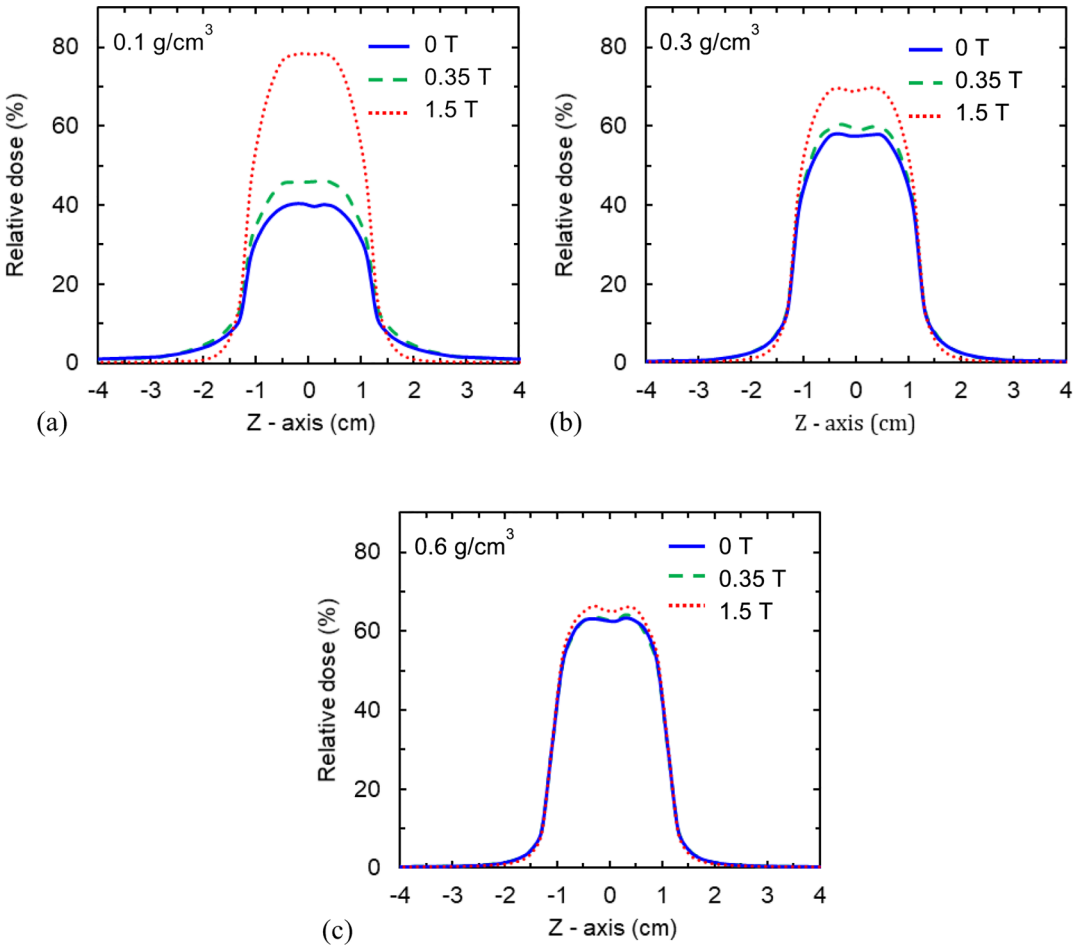

Fig. 13. Comparison of dose profiles by longitudinal magnetic fields for a 2 × 2 cm^2 field at SSD of 100 cm: densities of (a) 0.1 g/cm^3, (b) 0.3 g/cm^3, and (c) 0.6 g/cm^3 at a depth of 9 cm in a lung phantom. (Z-axis is defined in Fig. 1.)

secondary electrons obliquely entering the magnetic field direction draw a spiral trajectory along the beam axis [14]. In this case, the orbital radius of the secondary electrons is different from the gyro radius of the secondary electrons under the transverse magnetic field condition and is expressed by the following equation:

$$r = \frac{m(v \sin\theta)}{eB} \quad (0 < \sin\theta < 1) \tag{3}$$

where θ is the angle of incidence of secondary electrons in the longitudinal magnetic field. The gyro radius of secondary electrons in the longitudinal magnetic field condition becomes smaller than the orbital radius of the spiral trajectory along the longitudinal magnetic field, depending on the incident angle θ.

The trajectory of secondary electrons for 0 T spread to both sides of the lung. However, for the longitudinal magnetic field, secondary electrons are focused with the orbital radius of the spiral trajectory toward the central beam axis, as defined by Eq. (3). The larger the magnetic flux density, the smaller the orbital radius of the secondary electrons, as shown in Fig. 10(d)–(f). The spread of secondary electrons to both sides converges, and the dose near the beam axis increases. The effect of convergence of secondary electrons in this way is also called "electron focusing effect (EFE)" [26]. As a result, the spread of secondary electrons away from the irradiation field decreases, reducing the penumbra, as shown in Figs. 13 and 14. The dose increase near the center of the beam axis and the decrease in the penumbra are shown by various actual measurements [16,17]. In addition, the electron range is longer for lower densities and thus the dose enhancement is noticeable depending on the magnetic field parameters.

4.3. Dose distributions in lung tumor phantom

The lung tumor in the transverse magnetic field is prescribed by under dose and over dose at lung-tumor and tumor interfaces, respectively. Therefore, it needs to reduce the dose variation due to ERE by

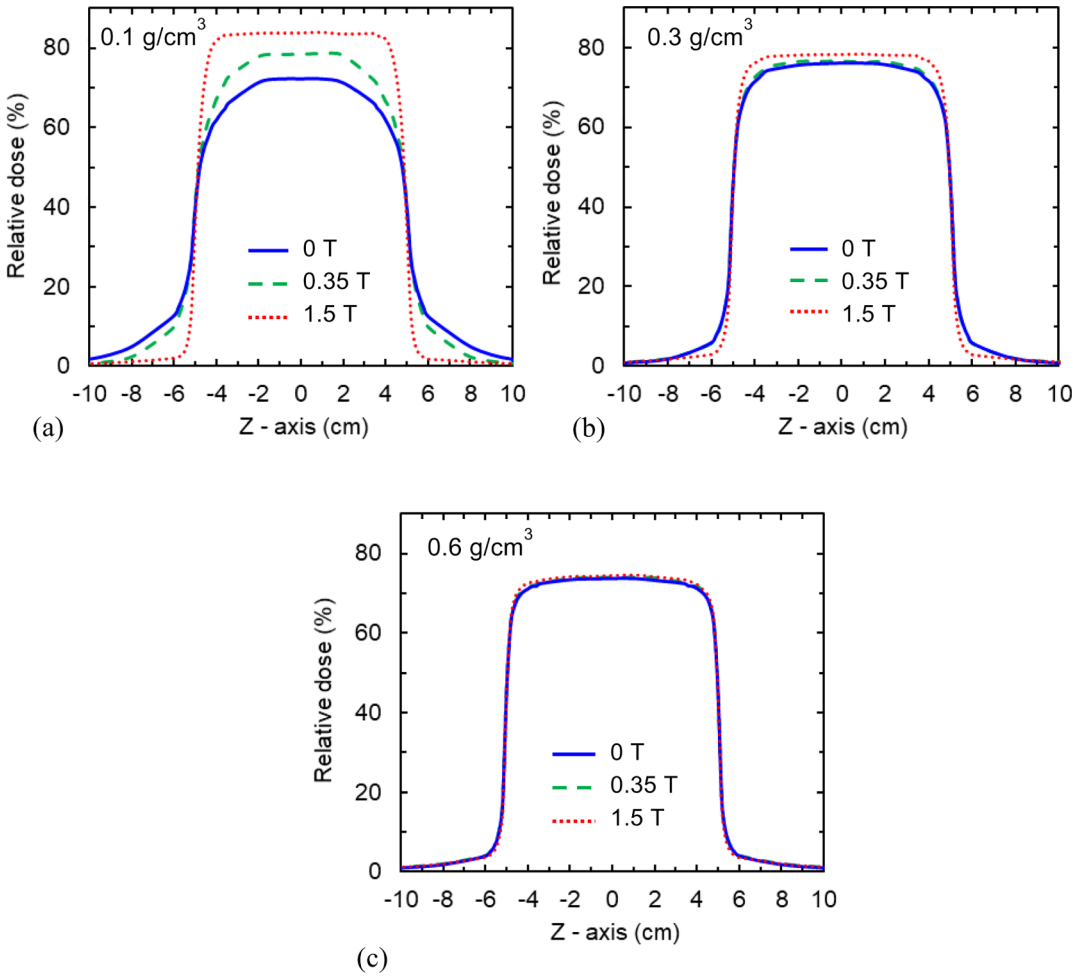

Fig. 14. Comparison of dose profiles by longitudinal magnetic fields for a 10 × 10 cm^2 field at SSD of 100 cm: densities of (a) 0.1 g/cm^3, (b) 0.3 g/cm^3, and (c) 0.6 g/cm^3 at a depth of 9 cm in a lung phantom. (Z-axis is defined in Fig. 1.)

Table 5
Comparison of penumbra at 9 cm depth in a lung phantom for 2 × 2 cm^2, 5 × 5 cm^2, and 10 × 10 cm^2 fields.

Density (g/cm^3)	Field size (cm^2)	Width of 80−20% (mm)		
		0 T	0.35 T	1.5 T
0.1	2 × 2	6.72	7.03 (+0.32)	5.08 (−1.64)
	5 × 5	11.46	11.22 (−0.24)	6.31 (−5.14)
	10 × 10	15.16	13.78 (−1.37)	7.13 (−8.03)
0.3	2 × 2	3.95	3.99 (+0.05)	3.50 (−0.45)
	5 × 5	5.49	5.55 (+0.07)	3.99 (−1.50)
	10 × 10	6.19	5.97 (−0.22)	4.45 (−1.75)
0.6	2 × 2	2.78	2.76 (−0.02)	2.67 (−0.11)
	5 × 5	3.28	3.28 (± 0.00)	2.94 (−0.35)
	10 × 10	3.66	3.78 (+0.12)	3.24 (−0.43)

Table 6
Dose increase/decrease at the water–lung interface (W-L), lung center (LC), and lung–water (L-W) interface in the longitudinal magnetic flux density for field sizes compared to 0 T. magnetic field conditions to 0 T.

Field (cm^2)	Magnetic flux density (T)	Density (g/cm^3)	Dose increase/decrease for 0 T		
			W-L	LC	L-W
2 × 2	0.35	0.1	0.0	15.5	7.4
		0.3	0.4	2.7	0.9
		0.6	−1.1	0.2	−0.4
	1.5	0.1	10.2	97.0	59.4
		0.3	2.7	20.8	11.9
		0.6	0.9	4.2	3.6
5 × 5	0.35	0.1	2.0	15.2	8.1
		0.3	−0.1	0.3	1.2
		0.6	−0.6	−0.2	−1.0
	1.5	0.1	4.3	73.3	55.2
		0.3	−0.3	6.2	5.1
		0.6	0.0	2.1	0.5
10 × 10	0.35	0.1	−0.9	7.1	5.9
		0.3	0.0	0.5	0.8
		0.6	−0.1	−1.4	0.2
	1.5	0.1	4.1	18.0	11.8
		0.3	−1.5	3.4	2.2
		0.6	0.7	0.8	−0.2

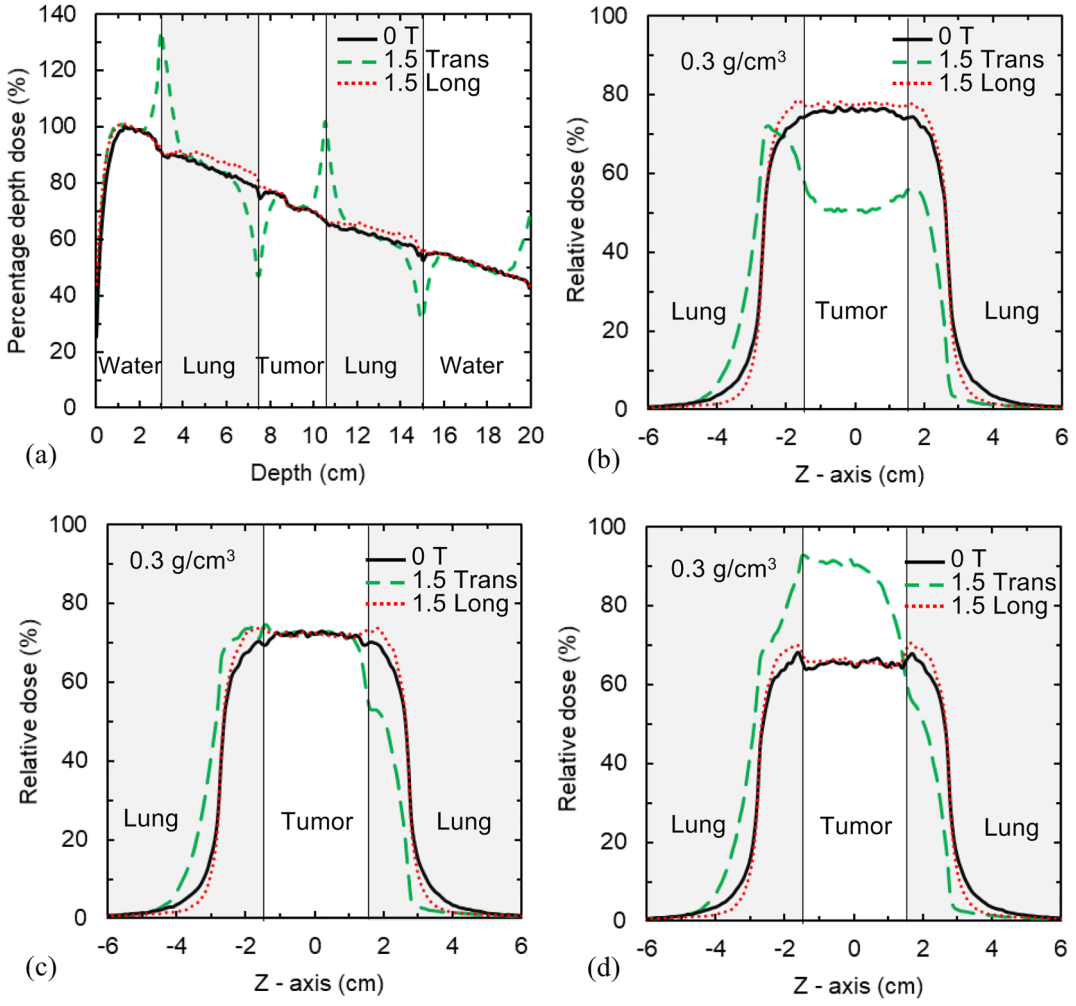

Fig. 15. Comparison of dose distributions in transverse and longitudinal magnetic fields of 0 T and 1.5 T for a 5 × 5 cm^2 field in a lung tumor phantom at SSD of 100 cm: (a) percentage depth dose curves and dose profiles: (b) lung-tumor interface, (c) tumor center and (d) tumor-lung interface. (Z-axis is defined in Fig. 1.)

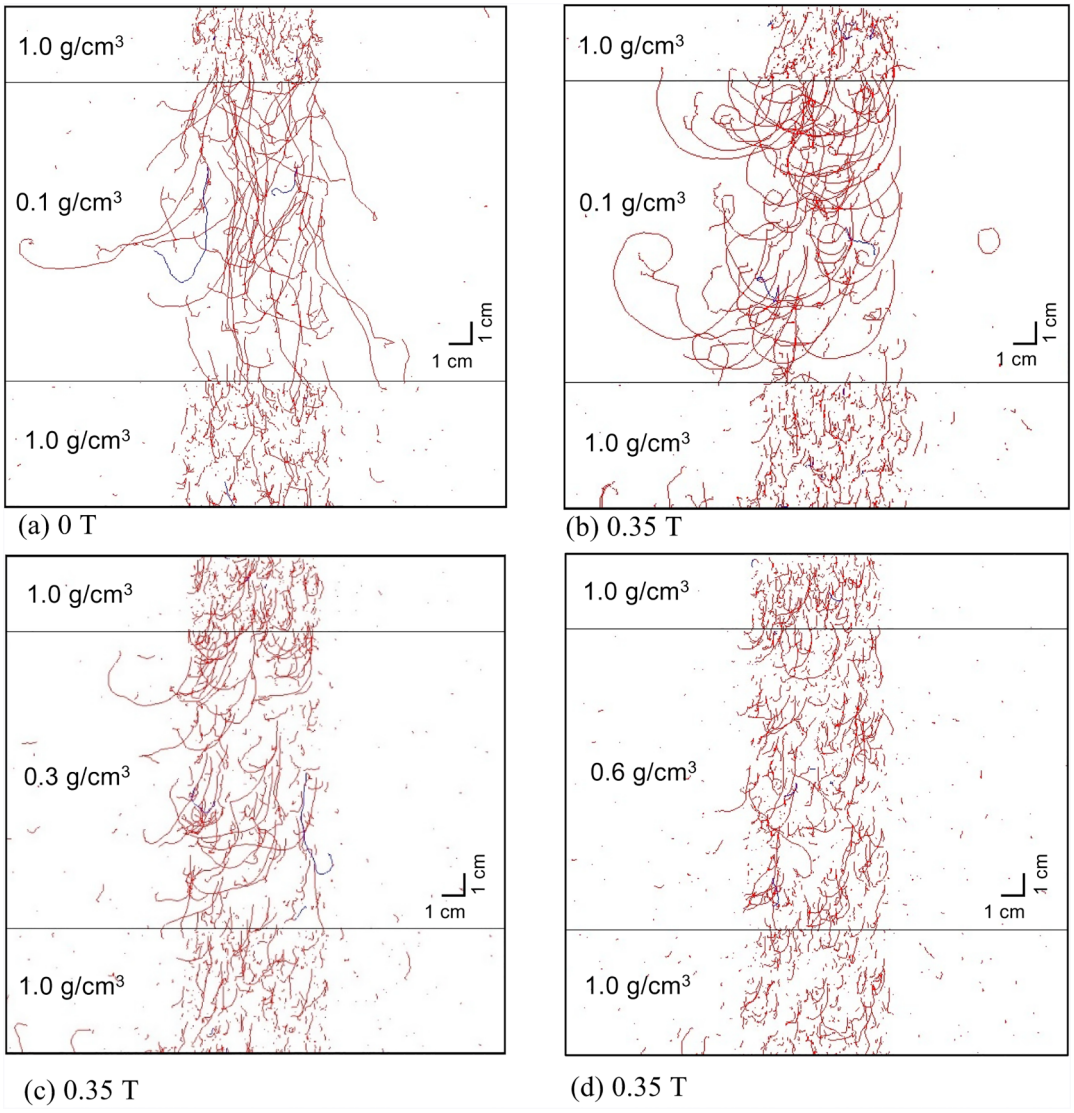

Fig. 16. Secondary electron trajectories in a lung phantom for transverse magnetic flux density of 0.35 T for a 5 × 5 cm^2 field. (a) 0 T, 0.1 g/cm^3, (b) 0.35 T, 0.1 g/cm^3, (c) 0.35 T, 0.3 g/cm^3, and (c) 0.35 T, 0.6 g/cm^3. The horizontal lines are the water–lung interface and the lung–water interface.

multidirectional irradiations for clinical implementation. In contrast, the tumor dose in longitudinal magnetic field is enhanced by EFE in lung and consequently the penumbra also reduces. The EFE for the lung tumor is expected to be usefully with decreasing the field size and increasing magnetic flux density.

5. Conclusions

The dose distributions are more affected by the magnetic field in lower density regions. For transverse magnetic fields, the dose at the water–lung interface and exit surface enhances as a consequence of the Lorentz force, whereas the dose at the lung–water interface is reduced. In addition, the dose profiles in lower density regions are further distorted by the Lorentz force depending on magnetic flux density. The depth dose in longitudinal magnetic fields is enhanced by the Lorentz force action, thus reducing the penumbra. This tendency is much more evident for lower densities, a smaller field, and higher magnetic strength. In this study, it was found that the influence of the magnetic field on dose distributions is changed by the magnetic strength, field size, and the density difference in lowdensity materials such as lungs. Since this study does not focus for dose distributions in a buildup region, it is important to evaluate the surface dose under the magnetic field using phase space data with the electron contamination from the linac head.

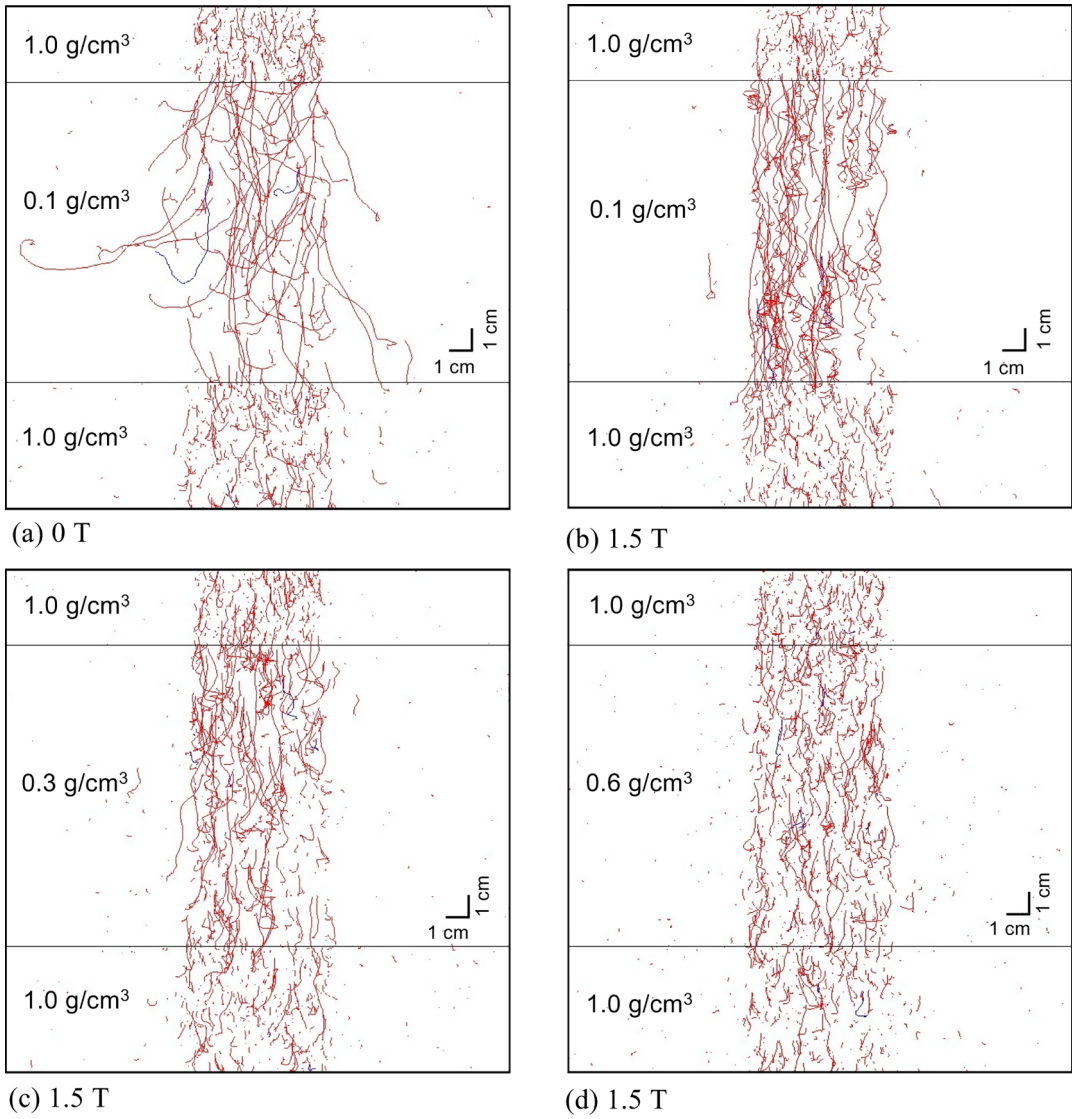

Fig. 17. Secondary electron trajectories in a lung phantom for a longitudinal magnetic flux density of 1.5 T for a 5 × 5 cm^2 field. (a) 0 T, 0.1 g/cm^3, (b) 1.5 T, 0.1 g/cm^3, (c) 1.5 T, 0.3 g/cm^3, and (c) 1.5 T, 0.6 g/cm^3. The horizontal lines are water–lung interface and the lung–water interface.

References

[1] Mutic S, Dempsey JF. The ViewRay system: magnetic resonance-guided and controlled radiotherapy. Semin Radiat Oncol 2014;24:196–9.
[2] Lagendijk JJW, Raaymakers BW, Vulpen MV. The magnetic resonance imaging-linac system. Semin Radiat Oncol 2014;24:207–9.
[3] Raaijmakers AJE, Raaymakers BW, Lagendijk JJW. Magnetic-field-induced dose effects in MR-guided radiotherapy systems: dependence on the magnetic field strength. Phys Med Biol 2008;53:909–23.
[4] Raaijmakers AJE, Raaymakers BW, Lagendijk JJW. Integrating a MRI scanner with a 6 MV radiotherapy accelerator: dose increase at tissue air interfaces in a lateral magnetic field due to returning electrons. Phys Med Biol 2005;50:1363–76.
[5] Raaymakers BW, Raaijmakers AJE, Kotte ANTJ, Jette D, Lagendijk JJW. Integrating a MRI scanner with a 6 MV radiotherapy accelerator: dose deposition in a transverse magnetic field. Phys Med Biol 2004;49:4109–18.
[6] Yang YM, Bednarz B. Consistency evaluation between EGSnrc and Geant4 charged particle transport in an equilibrium magnetic field. Phys Med Biol 2013;58:N47–58.
[7] Ahmad SB, Sarfehnia A, Kim A, Wronski M, Sahgal A, Keller BM. Backscatter dose effects for high atomic number materials being irradiated in the presence of a magnetic field: a Monte Carlo study for the MRI linac. Med Phys 2016;37:4916–23.
[8] Ahmad SB, Sarfehnia A, Paudel MR, Kim A, Hissoiny S, Sahgal A, et al. Evaluation of a commercial MRI linac based Monte Carlo dose calculation algorithm with geant4. Med Phys 2016;43:894–907.
[9] Rubinstein AE, Liao Z, Melancon AD, Guindani M, Followill DS, Tailor RC, et al. Technical note: a Monte Carlo study of magnetic-field-induced radiation dose effects in mice. Med Phys 2015;42:5510–6.
[10] Fallone BG. The rotating biplanar linac-magnetic resonance imaging system. Semin Radiat Oncol 2014;24:200–2.
[11] Keall PJ, Barton M, Crozier S. The Australian magnetic resonance imaging-linac program. Semin Radiat Oncol 2014;24:203–6.
[12] Kirkby C, Stanescu T, Rathee S, Carlone M, Murray B, Fallone BG. Patient dosimetry for hybrid MRI-radiotherapy systems. Med Phys 2008;35:1019–27.
[13] Kirkby C, Murray B, Rathee S, Fallone BG. Lung dosimetry in a linac-MRI radiotherapy unit with a longitudinal magnetic field. Med Phys 2010;35:4722–32.
[14] Bielajew A. The effect of strong longitudinal magnetic fields on dose deposition from electron and photon beams. Med Phys 1993;20:1171–9.
[15] Aubin JS, Santos DM, Steciw S, Fallone BG. Effect of longitudinal magnetic fields on a simulated in-line 6 MV linac. Med Phys 2010;37:4916–23.
[16] Alnaghy SJ, Begg J, Causer T, Alharthi T, Glaubes L, Dong B, et al. Technical note: penumbral width trimming in solid lung dose profiles for 0.9 and 1.5 T MRI-Linac prototypes. Med Phys 2018;45:479–87.
[17] Oborn BM, Gargett MA, Causer TJ, Alnaghy SJ, Hardcastle N, Metcalfe PE, et al. Experimental verification of dose enhancement effects in a lung phantom from inline magnetic fields. Radiother Oncol 2017;125:433–8.
[18] Rosenblum LJ, Mauceri RA, Wellenstein DE, Thomas FD, Bassano DA, Raasch BN, et al. Density patterns in the normal lung as determined by computed tomography. Radiology 1980;137:409–16.
[19] Van Dyk J, Keane TJ, Rider WD. Lung density as measured by computerized tomography: implications for radiotherapy. Int J Radiat Oncol Biol Phys 1982;8:1363–72.

[20] Agostinelli S, Allison J, Amako K, Apostolakis J, Araujo H, Arce P, et al. Geant4-a simulation toolkit. Nucl Instrum Methods Phys Res A 2003;506:250–303.
[21] Allison J, Amako K, Apostolakis J, Araujo H, Arce P, Asai M, et al. Geant4 developments and applications. IEEE Trans Nucl Sci 2006;53:270–8.
[22] Allison J, Amako K, Apostolakis J, Arce P, Asai M, Aso T, et al. Recent developments in GEANT4. Nucl Instr Methods Phys Res Sect A 2016;835:186–225.
[23] Rogers DWO, Kawrakow I, Seuntjens JP, Walters BRB, Mainegra-Hing E. NRC user codes for EGSnrc. NRCC Rep PIRS-702 (Rev B) 2013;702:1–92.
[24] Tomiyama Y, Araki F, Ohno T, Hioki K. Three-dimensional gamma analysis of dose distributions in individual structures for IMRT dose verification. Radiol Phys Technol 2014;7(2):303–9.
[25] Onizuka R, Araki F, Ohno T, Nakaguchi Y, Kai Y, Tomiyama Y, et al. Accuracy of dose calculation algorithms for virtual heterogeneous phantoms and intensity-modulated radiation therapy in the head and neck. Radiol Phys Technol 2016;9:77–87.
[26] Liney GP, Whelan B, Oborn B, Barton M, Keall P. MRI-Linear accelerator radiotherapy systems. Clin Oncol 2018;30:686–91.